Spin-valley polarized transport in a field-controllable bilayer silicene superlattice

Guangqin Xiong, Duojia Wang , Fangjie Xu , Yuxuan Ma, Xin Li, Tingting Wei, and Yu Wang *

Department of Physics, Faculty of Science, Kunming University of Science and Technology, Kunming 650500, China

We have theoretically investigated the spin-valley asymmetric transport of massive Dirac fermions in the field-controllable bilayer silicene superlattices. The spin-valley dependent ballistic transmission, conductance, and polarization have been systematically calculated by formulating the scattering matrix method for the completed four-band low-energy effective Hamiltonian. Our results uncover that for a single valley transport, near-perfect spin polarization and its perfect switching could be efficiently modulated by the gate field engineering. Under the one-dimensional periodic field modulation, two types of flat bands with less dispersion and, importantly, the perfect contrast in the spin-dependent subbands are observed for the bilayer silicene superlattice. Together with its larger spin-orbit coupling and better stability, these spin-valley asymmetric characteristics engineered by the gate field indicate that the field-controllable bilayer silicene could be a potential component candidate to achieve a fully spin-valley polarized beam for quantum logic applications.

I. INTRODUCTION

The giant commercial achievements of silicon-based integrated technologies have stimulated extensive debates on the development of much smaller, faster, and more powerful electronic devices [1]. In its physical limitation, fabricating the electronic devices with few-layer or even monolayer silicon materials should be an appealing yet ultimate strategy [2]. Experimentally, following the successes in the fabrication of graphene [3], a monolayer of carbon atoms packed closely in a hexagonal comblike lattice, much effort has been also paid to the synthesis of the silicon analog of graphene, namely silicene [4]. In recent years, several groups have demonstrated the fabrication of monolayer and multilayer silicene [5–12] onto the metallic and semiconducting substrates, establishing the solid bases for the development of silicene-based electronic devices.

For the construction of silicene-based logic devices, besides the general charge degree of freedom, both spin and valley degrees of freedom have also been regarded as the potential information carriers for the spintronic (valleytronic) devices. In such devices, the logic operation is achieved by turning on or off the spin (valley) polarized beam. Thus, for those applications, the efficient generation, modulation, and detection of spin (valley) polarized transport are the fundamental issues to be solved. Up to now, together with its spin-valley locking [13], field-tunable local band gap [14,15], and stronger spin-orbit interaction, many spin-valley dependent transport as well as topological quantum states like the quantum spin Hall effect [16,17] could be accessed in the silicene nanosystems at some realistic temperatures. Based upon these experimental and theoretical demonstrations, it should be convincing that silicene might be a potential platform for the development of topological quantum devices and spin-valley logic devices [18]. Unfortunately, due to the inferior stability of monolayer silicene, the reported field-effect transistor could only be operated at room temperature for several minutes [19]. This implies that the stability of monolayer silicene might also be a killer for other appealing devices residing on the monolayer silicene.

Besides the monolayer silicene, bilayer silicene (BLS) is another type of silicene frequently observed in experiments [4,7]. Structurally, BLS can be regarded as the stack of two monolayer silicenes in some orders [20,21]. This feature makes BLS have some peculiar properties unshared by monolayer silicene [21,22]. For instance, due to the stack-dependent electronic structures, it has been theoretically predicted by Liu *et al.* [23] that the $d + id'$ chiral superconductivity is observable in BLS. Moreover, due to the stronger interlayer interaction, an enhanced buckling is observed for each sublayer of BLS [20]. For this reason, BLS has a stronger spin-orbit interaction and larger field-tunable local band gap [24], all of which are highly favorable to manipulate the charge, spin, and valley dependent transport in BLS. However, little attention has been previously concentrated onto the electronic transport in BLS systems.

To engineer the electronic properties of BLS, imposing the periodic potential modulations is an attractive scheme. This, as an example, can be experimentally achieved by depositing an array of gates on top of BLS. In such a configuration, the electrostatic modulation of periodically arranged gates can induce a spatially periodic potential for the electronic transport within the BLS plane, forming the so-called BLS superlattice. Unfortunately, although this scheme has been well employed to construct various superlattice modulations for monolayer silicene [25–29], demonstrating the formation of spin and valley dependent miniband structure [28] and enhanced valley-resolved thermoelectric transport [29], nothing has been shown for its BLS counterparts. Thus, given

*wyraul107@163.com

that the additional interlayer interaction of BLS and its better stability, it is highly desirable to uncover the electronic transport of BLS under the modulation of spatially periodic modulations.

In this work, we have theoretically investigated the electronic transport properties of the gate-tunable BLS superlattice. Our results demonstrate that (1) the ballistic transmission probability (T) is highly anisotropy and spin-valley dependent, even inducing the perfect contrast between the spin-valley dependent transport at the proper parameter window; (2) under the top gate modulation, the spin-valley dependent transport properties could be efficiently tailored, providing a desirable method to control the spin-valley polarized transport; (3) comparing to single gate modulation, electronic transport could be efficiently enhanced by superlattice modulation, indicating a multiple reversal of perfect spin-valley polarization; and (4) the calculated miniband structure is highly spin-valley dependent and field tunable, implying the existence of a new spin-valley dependent yet gapped Dirac point. These results indicate that the gate-induced BLS superlattice could be an efficient amplifier for the electronic transport and potential subunit for the achievement of fully spin and valley polarized transport.

The rest of this paper is organized as follows: In Sec. II we mainly explain the considered BLS superlattice and the scattering matrix method formulated from the completed four-band effective Hamiltonian of BLS; the results for single gate modulation are first explained in Sec. III for the comparisons while those for the BLS superlattice are shown in Sec. IV; in Sec. V we discuss the field-engineered miniband structure of the BLS superlattice and we summarize our work in Sec. VI.

II. MODEL AND METHOD

The schematic lattice structure of our considered BLS is depicted in Fig. 1(a), where one type of the silicon atom in the bottom layer, i.e., the A_2 site, is vertically bonded to the other type of silicon atom in the top layer, namely the B_1 site, while the other type of silicon atom in one sublayer is well located in the center of hexagonal lattice of another sublayer, forming the so-called Bernal stacking [20,21]. With such a configuration, there are four atoms, i.e., A_1, B_1, A_2, and B_2, in the unit cell of BLS, further giving rise to more interatomic interactions than monolayer silicene. Importantly, according to the first-principle calculations, an enhanced sublattice buckling (0.66 Å) and spin-orbit gap (10 meV) have been theoretically predicted due to the strong interlayer covalent interaction [24]. This provides a larger parameter window to access the spin-valley dependent transport in the BLS system. Moreover, to reasonably reproduce the band diagram determined from the first-principles calculations, the main tight-binding parameters for BLS have been suggested as $\gamma_0 = 1.13$ eV, $\gamma_1 = 2.025$ eV, $\gamma_2 = 0.152$ eV, and $\gamma_3 = 0.616$ eV [23,24].

Similarly to bilayer graphene, by neglecting the weaker interlayer skew hopping, i.e., γ_2 and γ_3, and with the basis function $\psi = [\psi_{A_1}, \quad \psi_{B_1}, \quad \psi_{A_2}, \quad \psi_{B_2}]^\dagger$, the low-energy electronic transport of BLS near the corner points (valleys) of the Brillouin region could be well described by the following
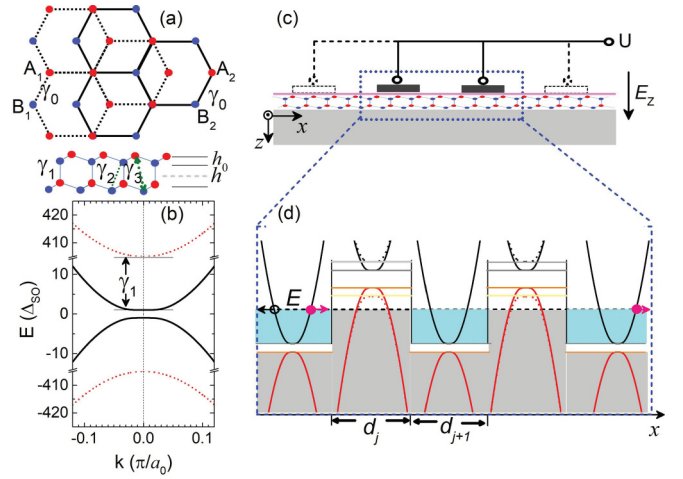
FIG. 1. The schematic structure of our considered BLS and gate-induced BLS superlattice. (a) The bottom view and side view of lattice structure for *AB*-stacked BLS with nearest intralayer hopping integral γ_0 and interlayer hopping integral γ_1, γ_2, and γ_3. (b) The representative band structure of *AB*-stacked BLS without the smaller γ_2 and γ_3, where $a_0 = 3.86$ Å is the lattice constant of BLS. (c) The sketched method to experimentally form BLS superlattice by means of periodically gate-biased BLS. (d) The representative band alignment of gate-induced BLS superlattice.

effective Hamiltonian [30], reading as

$$\hat{H} = \begin{bmatrix} U + \delta_2 & \hbar v_f k_- & 0 & 0 \\ \hbar v_f k_+ & U + \delta_1 & \gamma_1 & 0 \\ 0 & \gamma_1 & U - \delta_1 & \hbar v_f k_- \\ 0 & 0 & \hbar v_f k_+ & U - \delta_2 \end{bmatrix}, \quad (1)$$

where U is the electrostatic potential, $\hbar$ is the reduced Planck constant, $v_f \approx 0.55 \times 10^6$ m/s is the Fermi velocity, $k_\pm = k_x \pm i\eta k_y$ with $k_{x(y)}$ the x (y) component of two-dimensional momentum, and $\eta = \pm 1$ the valley index, i.e., plus (minus) for the K (K') valley. By referring to the vertical arrangement of the sublattice [the inset of Fig. 1(a)] and taking the baseline of the on-site potential at half of the interlayer separation (h), the gate field (E_Z) tunable $\delta_{1(2)}$ in Eq. (1) can be further expressed as

$$\delta_1 = \beta_1 \Delta_Z + \eta \sigma \Delta_{SO} \quad (2)$$

and

$$\delta_2 = \beta_2 \Delta_Z - \eta \sigma \Delta_{SO}, \quad (3)$$

where $\Delta_{SO} = 5$ meV [24] is the intrinsic spin-orbit coupling, $\sigma = \pm 1$ is the spin index with plus for the spin-up ($\Uparrow$) orientation and minus for the spin-down ($\Downarrow$) orientation, $\Delta_Z = hE_Z/2$ is the field-tunable staggered potential between A_2 site and B_1 site with the interlayer distance $h = 2.54$ Å, and by referring to the enhanced buckling height of each sublayer $h_0 = 0.66$ Å, β can be further written as $\beta_1 = 1$ while $\beta_2 = 1 + 2h_0/h$.

The energy spectra of BLS can be further determined from the Schrödinger equation $\hat{H}\psi = E\psi$ as

$$E = U + s\sqrt{\frac{\Gamma + l\sqrt{\Gamma^2 - 4\gamma_1^2\delta_2^2 - 4[(\hbar v_f k)^2 - \delta_1\delta_2]^2}}{2}} \quad (4)$$

with $s = \pm 1$ for the conduction (plus)/valence (minus) band, $l = \pm 1$ for the upper (plus)/lower (minus) band, $k = \sqrt{k_x^2 + k_y^2}$, and $\Gamma = \delta_1^2 + \delta_2^2 + 2(\hbar v_f k)^2 + \gamma_1^2$. Obviously, free of the electric modulation, i.e., $U = 0$ and $\Delta_Z = 0$, each calculated band has fourfold degeneracy. In this case, as depicted in Fig. 1(b), a sizable local gap $E_g \approx 2\Delta_{SO}$ could be traced between the lowest conduction and highest valence band while a much larger one, on the order of γ_1, between the lower and higher conduction (valence) band. Importantly, as can be concluded from Eq. (3), a nonzero U shifts the whole band diagram up and down while a nonzero Δ_Z can effectively enlarge or shut the local band gap. These features provide a flexible strategy to engineer various BLS quantum structures in an electrically controllable way.

As depicted in Fig. 1(c), we consider here the ballistic electronic transport in BLS plane under the modulation of top periodic gates, which can be experimentally achieved by depositing an array of metallic gates on top of BLS plane with a proper dielectric spacer. Each gate has a width d and is separated from its neighbors with a separation W. Thus, beneath the gate, the local band could be efficiently aligned by top gate modulation, forming a periodic potential to tailor the electronic transport in the BLS plane, i.e., x-y plane. Here to model the gate-induced periodic potential, as illustrated in Fig. 1(d), a rectangle-like profile is employed for simplicity, namely a constant $\Delta_Z(U)$ for the domains beneath the gates while zero for those uncovered by the gates.

By neglecting the possible intervalley scattering stimulated by the rectangle-like step potential [31], with a given gate modulation, in the jth domain, the resulting four-component spinor wave function can be derived as

$$\psi_j = \sum_{l,\pm} F_{j,\pm}^l \begin{pmatrix} \alpha_{j,\pm}^l \\ 1 \\ \rho_j^l \\ \beta_{j,\pm}^l \end{pmatrix} e^{\pm i k_{j,x}^l (x - x_{j-1}) + i k_y y} \tag{5}$$

with $\pm$ for the forward (plus) and backward (minus) state, x_j the location of the jth interface, $\alpha_{j,\pm}^l = \frac{\hbar v_f (\pm k_{j,x}^l - i\eta k_y)}{\varepsilon_j - \delta_2}$, $\beta_{j,\pm}^l = -\frac{(\varepsilon_j - \delta_2)\rho_j^l \alpha_{j,\mp}^l}{\varepsilon_j + \delta_2}$, $\rho_j^l = \frac{\varepsilon_j - \delta_1}{\gamma_1} - \frac{(\hbar v_f)^2 [(k_{j,x}^l)^2 + k_y^2]}{\gamma_1(\varepsilon_1 - \delta_2)}$, where $\varepsilon_j = E - U_j$, and the longitudinal wave vector $k_{j,x}^l$ can be further derived from Eq. (4) as

$$k_{j,x}^l = \sqrt{\frac{\varepsilon_j^2 + \delta_1 \delta_2 - l\sqrt{\gamma_1^2(\varepsilon_j^2 - \delta_2^2) + \varepsilon_j^2(\delta_1 + \delta_2)^2}}{\hbar^2 v_f^2} - k_y^2}. \tag{6}$$

Here since the translation invariant along the y direction is well conserved, k_y is a good quantum number and by referring to the value at the leads, can be explicitly written as

$$k_y = \frac{1}{\hbar v_f} \sqrt{E^2 - \Delta_{SO}^2 - l\sqrt{\gamma_1^2(E^2 - \Delta_{SO}^2)}} \sin\theta \tag{7}$$

with θ denoting the incident angle with respect to the x direction.

To determine the unknown coefficients $F_{j,\pm}^l$ in Eq. (5), the boundary condition governing the wave function continuity at each interface is employed. For example, at the jth interface,

the resulting relationship of the wave function between two neighboring domains is given by

$$\mathbf{G}_j \mathbf{P}_j^{-1} \begin{pmatrix} F_{j,+}^+ \\ F_{j,+}^- \\ F_{j,-}^+ \\ F_{j,-}^- \end{pmatrix} e^{i k_y y} = \mathbf{G}_{j+1} \begin{pmatrix} F_{j+1,+}^+ \\ F_{j+1,+}^- \\ F_{j+1,-}^+ \\ F_{j+1,-}^- \end{pmatrix} e^{i k_y y} \tag{8}$$

with

$$\mathbf{G}_j = \begin{bmatrix} \alpha_{j,+}^+ & \alpha_{j,+}^- & \alpha_{j,-}^+ & \alpha_{j,-}^- \\ 1 & 1 & 1 & 1 \\ \rho_j^+ & \rho_j^- & \rho_j^+ & \rho_j^- \\ \beta_{j,+}^+ & \beta_{j,+}^- & \beta_{j,-}^+ & \beta_{j,-}^- \end{bmatrix}, \tag{8a}$$

$$\mathbf{P}_j = \begin{bmatrix} e^{-i k_j^+ d_j} & 0 & 0 & 0 \\ 0 & e^{-i k_j^- d_j} & 0 & 0 \\ 0 & 0 & e^{i k_j^+ d_j} & 0 \\ 0 & 0 & 0 & e^{i k_j^- d_j} \end{bmatrix}. \tag{8b}$$

Obviously, the column vector $\mathbf{F}_j$ in the jth domain can be easily related to those for $(j+1)$th counterparts as

$$\mathbf{F}_j = \mathbf{P}_j \mathbf{M}_{j,j+1} \mathbf{F}_{j+1} \tag{9}$$

with $\mathbf{M}_{j,j+1} = \mathbf{G}_j^{-1} \mathbf{G}_{j+1}$. Here in order to calculate the transport properties like T and conductance (G) in a much more stable feature, the scattering matrix method [32,33] is employed. For this purpose, both $\mathbf{P}_j$ and $\mathbf{M}_{j,j+1}$ are rewritten in the form of the block matrix as

$$\mathbf{M}_{j,j+1} = \begin{bmatrix} \mathbf{M}_A(j, j+1) & \mathbf{M}_B(j, j+1) \\ \mathbf{M}_C(j, j+1) & \mathbf{M}_D(j, j+1) \end{bmatrix}, \tag{10}$$

where each $\mathbf{M}_\tau(j, j+1)$ is a 2×2 block matrix with the subscript $\tau = A, B, C$, and D. Correspondingly, $\mathbf{P}_j$ is rewritten as

$$\mathbf{P}_j = \begin{bmatrix} \mathbf{P}_{F,j} & 0 \\ 0 & \mathbf{P}_{R,j} \end{bmatrix} \tag{11}$$

with

$$\mathbf{P}_{F,j} = \begin{bmatrix} e^{-i k_{j,x}^+ d_j} & 0 \\ 0 & e^{-i k_{j,x}^- d_j} \end{bmatrix}, \tag{11a}$$

$$\mathbf{P}_{R,j} = \begin{bmatrix} e^{i k_{j,x}^+ d_j} & 0 \\ 0 & e^{i k_{j,x}^- d_j} \end{bmatrix}. \tag{11b}$$

With this rewritten form, the coefficients of forward state $\mathbf{F}_{j,+}^l = [F_{j,+}^+ \quad F_{j,+}^-]^\dagger$ are separated from those for the backward states $\mathbf{F}_{j,-}^l = [F_{j,-}^+ \quad F_{j,-}^-]^\dagger$. Unlike Eq. (9) for the transfer matrix method, in the framework of the scattering matrix (**S**) method, the coefficients in the $(j+1)$th region should be related to those for the incident lead ($j = 0$ or L) as

$$\begin{bmatrix} \mathbf{F}_{j+1,+}^l \\ \mathbf{F}_{L,-}^l \end{bmatrix} = \begin{bmatrix} \mathbf{S}_A(L, j+1) & \mathbf{S}_B(L, j+1) \\ \mathbf{S}_C(L, j+1) & \mathbf{S}_D(L, j+1) \end{bmatrix} \begin{bmatrix} \mathbf{F}_{L,+}^l \\ \mathbf{F}_{j+1,-}^l \end{bmatrix}, \tag{12}$$

where each $\mathbf{S}_\tau$ ($\tau = A, B, C, D$) is also a 2×2 block matrix, which, by combining with Eq. (9), can be explicitly derived

from those for the jth region via the following iterative expression, reading as

$$
\begin{aligned}
\mathbf{S}_A(L, j+1) &= \{\mathbf{P}_{F,j}\mathbf{M}_A(j, j+1) - \mathbf{S}_B(L, j)\mathbf{P}_{R,j} \\
&\quad \times \mathbf{M}_C(j, j+1)\}^{-1}\mathbf{S}_A(L, j), \qquad (12a)
\end{aligned}
$$

$$
\begin{aligned}
\mathbf{S}_B(L, j+1) &= \{\mathbf{P}_{F,j}\mathbf{M}_A(j, j+1) - \mathbf{S}_B(L, j)\mathbf{P}_{R,j} \\
&\quad \times \mathbf{M}_C(j, j+1)\}^{-1}\mathbf{S}_B(L, j)\mathbf{P}_{R,j} \\
&\quad \times \mathbf{M}_D(j, j+1) - \mathbf{P}_{F,j}\mathbf{M}_B(j, j+1),
\end{aligned}
$$
$$(12b)$$

$$
\begin{aligned}
\mathbf{S}_C(L, j+1) &= \mathbf{S}_C(L, j) + \mathbf{S}_D(L, j)\mathbf{P}_{R,j}\mathbf{M}_C(j, j+1) \\
&\quad \times \mathbf{S}_A(L, j+1), \qquad (12c)
\end{aligned}
$$

$$
\begin{aligned}
\mathbf{S}_D(L, j+1) &= \mathbf{S}_D(L, j)\mathbf{P}_{R,j}\mathbf{M}_C(j, j+1)\mathbf{S}_B(L, j+1) \\
&\quad + \mathbf{S}_D(L, j)\mathbf{P}_{R,j}\mathbf{M}_D(j, j+1). \qquad (12d)
\end{aligned}
$$

Thus, starting from the initial condition $\mathbf{S}_A(L, L) = \mathbf{S}_D(L, L) = \mathbf{I}_2$ and $\mathbf{S}_B(L, L) = \mathbf{S}_C(L, L) = \mathbf{0}$, the total scattering matrix $\mathbf{S}(L, R)$ that relates the left lead to the right lead can be determined. The resulting spinor-resolved transmission probability $T_{\eta,\sigma}^{l,l'}$ can thus be expressed as

$$
T_{\eta,\sigma}^{l,l'} = \frac{k_{R,x}^{l'}}{k_{L,x}^{l}}\left|S_A^{l,l'}(L, R)\right|^2. \qquad (13)
$$

Under the zero-temperature regime, the concerned spinor-resolved ballistic conductance $G_{\eta,\sigma}^{l,l'}$ can be further determined from the Landauer-Büttiker formula as

$$
G_{\eta,\sigma}^{l,l'} = G_0 \int_{-\pi/2}^{\pi/2} T_{\eta,\sigma}^{l,l'}(E, \theta)\cos\theta\, d\theta, \qquad (14)
$$

where $G_0 = \frac{e^2 L_y}{\pi^2\hbar^2 v_f}\sqrt{E^2 - \Delta_{so}^2 + \sqrt{\gamma_1^2(E^2 - \Delta_{so}^2)}}$ is the taken conductance unit with e the elementary charge and L_y the transverse length of the system.

Indeed, for the considered pure electric modulation in our two-terminal configuration, as can be concluded from the model Hamiltonian, due to the emerging degeneracy for $\hat{H}(\eta, \sigma)$, i.e., $\hat{H}(K, \Uparrow) = \hat{H}(K', \Downarrow)$ while $\hat{H}(K, \Downarrow) = \hat{H}(K', \Uparrow)$, no net spinor-polarized transport should be observed for both spin and valley index. Thus to uncover the fundamental effect of pure electric modulation on electronic transport of BLS, the single-valley transport, e.g., the K valley, is sampled while those for the K' valley could be easily obtained by only reversing the sign. Following this approximation, the resulting spin polarization $P_s^{l,l'}$ could be further uncovered as

$$
P_s^{l,l'} = \frac{G_{K,\Uparrow}^{l,l'} - G_{K,\Downarrow}^{l,l'}}{G_{K,\Uparrow}^{l,l'} + G_{K,\Downarrow}^{l,l'}}. \qquad (15)
$$

In principle, since two bands are evolved into our model, four $T_{\eta,\sigma}^{l,l'}$, two for intraband transport and two for the interband transport, should be accessible as those for bilayer graphene [30], for which the interlayer coupling is only on the order of ~ 0.4 eV. However, due to the much larger interlayer coupling (~ 2.02 eV) of BLS, the bottom of the upper band approaches almost the top of the lower band. This implies, for the realistic modulation and carrier concentration in the experimentally accessible BLS [4], the expected intraband transport for the
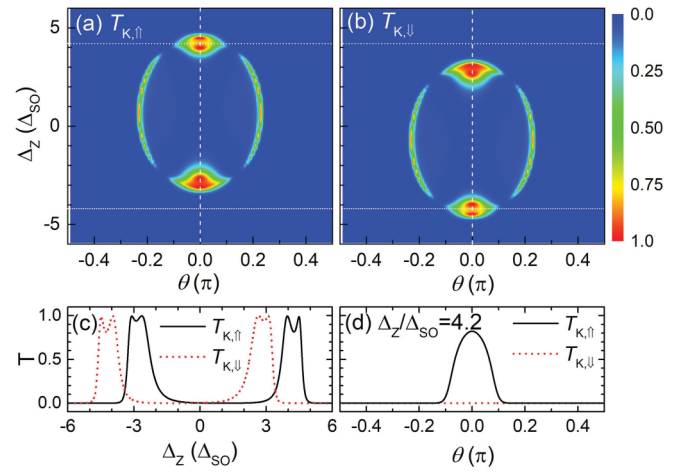
FIG. 2. The tunneling characteristic of massive Dirac fermion near the K valley of lower band through a single gate-induced BLS barrier. Top panel for the contour plot of $T_{K,\Uparrow}$ (a) and $T_{K,\Downarrow}$ (b) as a function of Δ_Z and θ. (c) The specific comparison of Δ_Z-dependent $T_{K,\Uparrow}$ (solid line) and $T_{K,\Downarrow}$ (short-dashed line) with $\theta = 0$ [vertical dashed line in (a) and (b)]. (d) The direct comparison of θ-dependent $T_{K,\Uparrow}$ (solid line) and $T_{K,\Downarrow}$ (short-dashed line) with $\Delta_Z = 4.2\Delta_{SO}$ [top dotted line in (a) and (b)].

upper band and two interband transports are negligible. Thus, in the subsequent sections, only the intraband transport for the lower band is concerned and, for brevity, the superscripts, l and l', for all concerned transport properties have been removed, namely $T_{\eta,\sigma}^{l,l'} \to T_{\eta,\sigma}$, $G_{\eta,\sigma}^{l,l'} \to G_{\eta,\sigma}$, and $P_s^{l,l'} \to P_s$.

III. SINGLE BARRIER

Prior to directly showing the transport properties for the BLS superlattice, in this section a single gate-induced modulation is first analyzed to uncover the underlying physics for the spinor-dependent transport. Physically, as shown in Fig. 1, under the Δ_Z modulation, the resulting BLS barrier is spinor dependent, which can make the transport be spin asymmetric for a specific valley. By sampling the K valley ($\eta = 1$), the illustrative spin-dependent $T_{K,\Uparrow(\Downarrow)}$ is depicted in Fig. 2 as a function of θ and Δ_Z with $d = 10$ nm, $E = 10\Delta_{SO}$, and $U = 16\Delta_{SO}$. As shown in Fig. 2(a) for the spin-up state, free of the Δ_Z modulation, the observed $T_{K,\Uparrow}$ is highly anisotropic, only showing symmetrically a finite value around $\theta = 0.22\pi$ while a prohibitive feature for the rest. By increasing Δ_Z, the required θ for the pronounced transmission is also changed, displaying an arc-shaped evolution. Importantly, for the proper Δ_Z, the perfect transmission, i.e., $T_{K,\Uparrow} = 1$, is highly localized around $\theta = 0$. This implies that the gate modulation should be an effective strategy to construct a beam collimator for the silicene-based quantum devices. More interestingly, as evidenced in Fig. 2(a), an asymmetric response of $T_{K,\Uparrow}$ is clearly observed for the Δ_Z modulation. Thus, for the same field strength, only reversing the direction of gate field can give rise to giant difference in the transmission properties. Specifically, with $\theta = 0$, the perfect transmission could be observed for $\Delta_Z = -3.0\Delta_{SO}$ while a prohibitive scenario for $\Delta_Z = 3.0\Delta_{SO}$. This asymmetric response enables the con-
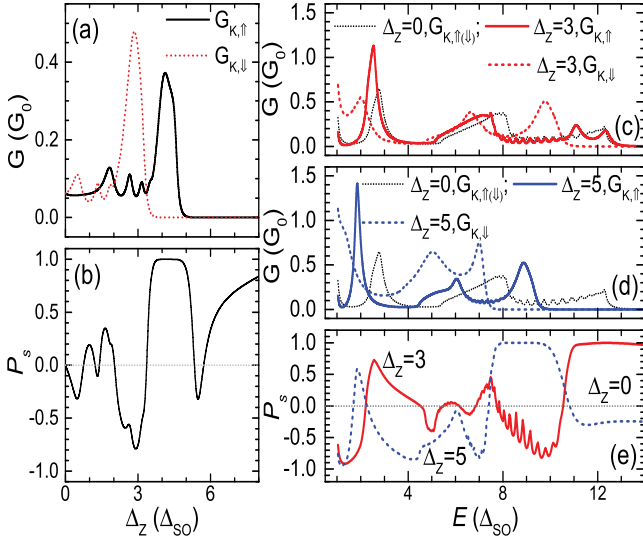
FIG. 3. The conductance G (a) and resulting spin polarization P_s (b) as a function of Δ_Z. In the right column the comparisons of spin-resolved G-E spectra between zero and finite field modulation, (c) for $\Delta_Z = 3\Delta_{SO}$ and (d) for $\Delta_Z = 5\Delta_{SO}$; while in (e) the resulting P_s-E spectra are compared.

struction of a quantum switch for a fully spinor-polarized beam by only reversing the orientation of the gate field.

For the other spin state, as shown in Fig. 2(b), the similar θ and Δ_Z dependent evolutions are well observed, but the calculated contour plot has been reversed vertically, making the two plots be symmetric with respect to the zero-field condition. To see this point more clearly, we have sampled the cases with $\theta = 0$, corresponding to the vertical dashed line in (a) and (b), and explicitly depicted in Fig. 2(c) with T as a function of Δ_Z for both spin states. It is easily observed that, by modifying Δ_Z, the pronounced T for different spin states emerges at different Δ_Z. For the spin-up state (solid line), the proper Δ_Z/Δ_{SO} should be controlled either in the range of $-3.6 \sim -1.5$ or in the range of $3.2 \sim 4.6$, while for the spin-down state (short-dashed line), the corresponding ranges are $-4.6 \sim -3.2$ and $1.5 \sim 3.6$. Evidently, two spin-resolved branches are in fact symmetric with respect to the zero point, showing $T_{K,\Uparrow}(\Delta_Z) = T_{K,\Downarrow}(-\Delta_Z)$. Owing to these asymmetric responses of T at a given Δ_Z, the desirable spin-polarized transport can thus be accessed under the gate field modulation once a single-valley transport is achieved. For instance, as clearly depicted in Fig. 2(d) for $\Delta_Z = 4.2\Delta_{SO}$, transport for the spin-up state is fully prohibitive in the whole forward space while conserving a pronounced value for the spin-down state with θ ranging from -0.1π to 0.1π. By further modulating Δ_Z, near-perfect contrast, namely $T = 1$ for one spin state while 0 for the other, could be expected, which is highly favorable for the spin-polarized transport.

In Fig. 3(a) the corresponding conductance G is further depicted as a function of Δ_Z for both spin states. It is remarkably seen that, with increasing Δ_Z, G for both spin states shows initially some visible oscillation with a small amplitude, then approaches a peak under the proper Δ_Z, and finally reduces to zero for the large enough Δ_Z due to the evanescent

mode-dominated transport beneath the gate. Importantly, due to the Δ_Z-induced spin-dependent barrier, the observed G-Δ_Z spectra are also spin dependent. This feature enable us to observe the fully polarized spin transport under the proper Δ_Z modulations. For instance, in Fig. 3(a), for Δ_Z in the range of $3.8\Delta_{SO}$ to $4.8\Delta_{SO}$, G for the spin-up state has a pronounced value while that for the spin-down state is fully prohibited. Consequently, within this range, the resulting spin polarization P_s can be up to 100% as explicitly depicted in Fig. 3(b). Below this range, although some pronounced P_s can also be traced, its visible oscillation might be less attractive for the spin-logic applications, while beyond this range, large P_s with less oscillation could be well observed, but the corresponding G are negligible for both spin states, which is also unfavorable for the realistic applications.

Figures 3(c) and 3(d) further compare the spin-dependent G-E spectra for the finite Δ_Z modulation, (c) for $\Delta_Z = 3\Delta_{SO}$, and (d) for $\Delta_Z = 5\Delta_{SO}$, with those for $\Delta_Z = 0$. It is evidently viewed that the G-E spectra for zero Δ_Z are spin independent due to the vanishing spin-dependent barrier, while for the nonzero Δ_Z, G become spin dependent, showing some spin-dependent G peaks at different E. Importantly, at these cases, as can be seen from the G-E spectra, there are several E regions showing a finite G for one spin state while a prohibited value for the other, implying different spin-polarized transports could be expected for different energy states. Thus, as depicted in Fig. 3(e) for the resulting P_s, the multiple reversal in P_s can be observed, and with increasing Δ_Z the appealing near-perfect P_s platform has been lowered from $E/\Delta_{SO} = 11 \sim 13$ for $\Delta_Z = 3\Delta_{SO}$ to $8 \sim 10$ for $\Delta_Z = 5\Delta_{SO}$. This electric-controllable strategy in tailoring the spinor-dependent transport is highly favorable for the BLS-based quantum logic applications.

IV. BLS SUPERLATTICES

To further enhance the spinor-dependent transport, increasing the number of top gates and inducing the multiple BLS barriers might be an effective strategy. By sampling $\theta = 0$, Fig. 4 depicts the spin-dependent T as a function of Δ_Z under the modulation of multiple BLS barriers with $d = W = 10$ nm, $E = 10\Delta_{SO}$, and $U = 16\Delta_{SO}$. It is evidently observed that, with increasing n, the lower threshold of the T band for the spin-down state has been slightly shifted toward larger Δ_Z, while that for the higher counterpart is oppositely shifted toward lower Δ_Z. For the spin-up state, a much weaker but similar evolution is conserved. Due to this asymmetric displacement, the T band for both spins has been slightly narrowed, making two spin-dependent bands be well separated. Comparing to single barrier, this enhanced separation of spin-dependent T band for multiple barriers might be favorable to observe the perfect switch of spin-polarized beam. Indeed, beside this near-perfect T band, an additional T band, consisting of a series of T peaks induced by the quantum well resonance, can be also traced for the spin-down state in the prohibitive zone of the single gate modulation. Moreover, unlike the spin-down state, the increasing n induces much stronger oscillation in the observed T band for the spin-up state, having a series of better-resolved T peaks. From these observations,
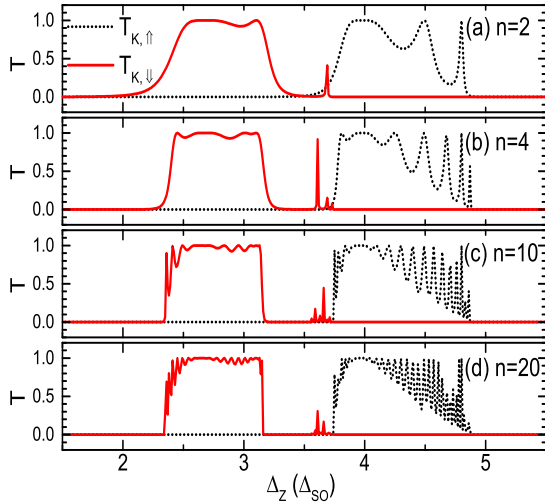
FIG. 4. The spin-dependent T as a function of Δ_Z with $d = W = 10$ nm, $E = 10\Delta_{SO}$, $U = 16\Delta_{SO}$, and $\theta = 0$. In each panel, the number of BLS barriers n has also been marked.

the enhanced modulation of spin-dependent transport should be convinced for the multiple BLS barriers.

Still with $E = 10\Delta_{SO}$ and $U = 16\Delta_{SO}$, in Fig. 5 the specific conductance G (left panel) and resulting spin polarization P_s (right panel) are depicted as a function of Δ_Z for several representative BLS superlattices. As shown in Fig. 5(a1) for $n = 10$ and $d = W = 10$ nm, with the increasing Δ_Z, the evolution of G for both spin states is highly similar to that for $n = 1$ [see Fig. 2(c)]; e.g., the remarkable G bands for both spin states are still well located in the range of $\Delta_Z/\Delta_{SO} = 2.4 \sim 3.2$ for spin-down state while $3.6 \sim 4.5$ for spin-up state. Due to the multiple modulation of BLS barriers, much stronger oscillation with more visible conductance peaks could be easily observed in the obtained G-Δ_Z spectra. Importantly, unlike the single barrier, the improving Δ_Z for multiple barriers induces several attractive windows that has a
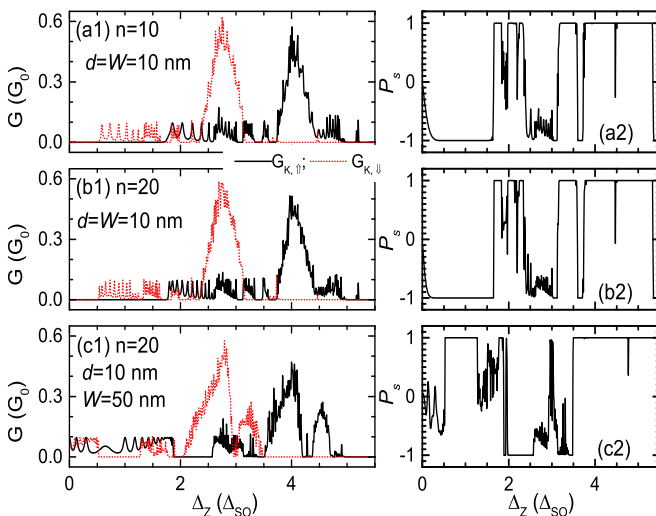
FIG. 5. The conductance G (left panel) and resulting spin polarization P_s (right panel) as a function of Δ_Z for the shown BLS superlattices.

near-zero conductance for one spin state while an observable value for the other state. Owing to this spin-dependent contrast, as can be seen from Fig. 5(a2), several perfect platforms with spin polarization up to 100% could be easily traced. For instance, for $\Delta_Z/\Delta_{SO} = 3.2 \sim 3.6$ and $3.8 \sim 4.4$, a fully polarized beam should be accessed for the spin-up state. Furthermore, it is also observed that, under the Δ_Z modulation, several perfect transitions unshared by single barrier, namely reversing the fully polarized spin beam from one spin state to the other, could also be observed, making the construction of the electric-controllable spin switch in the BLS system be highly expectable.

As a control case, by further increasing n up to 20, Fig. 5(b1) depicts the corresponding G as a function of Δ_Z. It is observed that, besides denser G peaks in the derived G-Δ_Z spectra, the whole evolutions of G are almost identical to those for $n = 10$ for both cases. Thus as can be seen from Fig. 5(b2) for the resulting P_s, a similar response could be traced when comparing to that for $n = 10$. The increasing n only induces the enhanced oscillations for Δ_Z/Δ_{SO} ranging from 2.4 to 3.1. Thus, to reasonably access spin-dependent transport in the biased BLS nanostructures, only a finite number of BLS barriers should be employed.

However, differently from the n-insensitive modulation, the evolution of G is strongly sensitive to its cell size. As evidenced in Fig. 5(c1) with $n = 20$, by increasing the separation of top gates, i.e., the well width W of a unit cell, from 10 nm to 50 nm, more well separated G bands could be explicitly observed for each spin state. This can be ascribed to the formation of more spin-dependent quantum well states induced by the quantum-size effect. Attractively, due to the misalignment of spin-dependent G-Δ_Z spectra, more desirable Δ_Z windows, namely a visible G for one spin state while a prohibited value for the other, could be well traced. Consequently, as shown in Fig. 5(c2), the corresponding P_s displays also more appealing regions for perfect spin polarization and perfect polarization switching. Different from the spin-dependent evanescent transport for a single barrier, these observations indicate that the transport through the spin-resolved minibands is a dominant mechanism for the multiple barriers. When the carrier transport is well located in the miniband for one spin state while out for the other, a perfect spin polarization could be observed. By switching the in-band transport for spin states, the perfect transition could be further traced. Thus, for a proper BLS superlattice, multiple perfect reversals of the spin-polarized state could be easily achieved by carefully tuning the strength of the gate field.

V. SUPERLATTICE SUBBANDS

Having seen the attractive spin-dependent transport through the finite BLG barriers, in this section the specific subband structures of the rigorous BLS superlattice are further analyzed. This can be performed by applying the Kronig-Penney model [34] for the structure depicted in Fig. 1(d). Due to the one-dimensional periodical modulation, the system wave function should be taken in the form of Bloch's wave function, reading as

$$\psi(x + \Lambda) = e^{iK_x\Lambda}\psi(x), \quad (16)$$
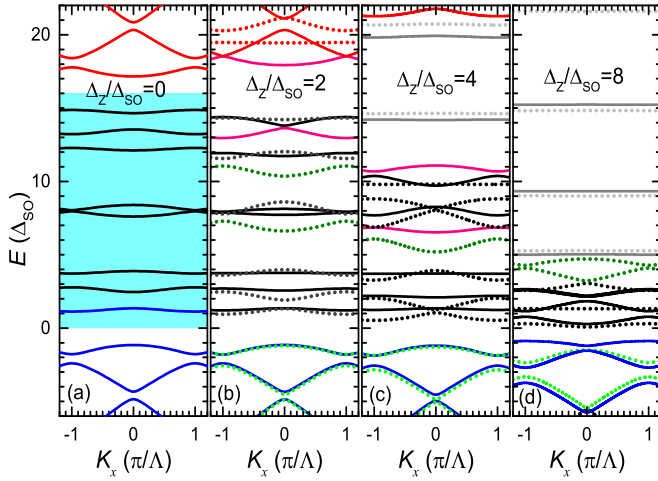
FIG. 6. The subbands of BLS superlattice with $d = W = 10$ nm under different Δ_Z modulation: (a) $\Delta_Z/\Delta_{SO} = 0$, (b) $\Delta_Z/\Delta_{SO} = 2$, (c) $\Delta_Z/\Delta_{SO} = 4$, and (d) $\Delta_Z/\Delta_{SO} = 8$, where solid lines are for spin-up state while dotted lines for spin-down state.

where K_x is the Bloch wave vector and $\Lambda = d + W$ is the length of the unit cell. By combining with Eq. (16) and the spinor wave function, i.e., Eq. (5), for the barriers and wells, as sampled in Fig. 1(d), matching the wave function at the boundary $x = m\Lambda + d$ and $x = (m + 1)\Lambda$, one can obtain the following matrix equation, given by

$$\begin{bmatrix} \mathbf{G}_W & -\mathbf{G}_B \\ \mathbf{G}_W \mathbf{P}_W^{-1} & -\mathbf{G}_B \mathbf{P}_B e^{iK_x\Lambda} \end{bmatrix} \begin{bmatrix} \mathbf{F}_W \\ \mathbf{F}_B \end{bmatrix} = 0, \qquad (17)$$

where the corresponding submatrices $\mathbf{G}_{W(B)}$ and $\mathbf{P}_{W(B)}$ are respectively the same as Eqs. (8a) and (8b) with the subscript W (B) denoting the well (barrier) region, while $\mathbf{F}_{W(B)}$ is the same column vector as shown in Eq. (8) for the well (barrier). Starting from Eq. (17), the concerned subband dispersion could be numerically determined from the condition governing the determinant of the coefficient matrix being zero through the Newton method. In Fig. 6 the specific subband dispersion of the BLS superlattice is explicitly depicted for different Δ_Z by taking $d = W = 10$ nm and $U = 16\Delta_{SO}$. As shown in Fig. 6(a) for zero Δ_Z, within the confined regime (gray-colored block), the whole structure could be regarded as a cascaded structure of the n-p junction and seven gapped subbands are observable with three negative-bowing subbands and four positive-bowing subbands. Depending on the order of subbands, different gaps could be observed for two neighboring subbands. For instance, near $E/\Delta_{SO} = 8$, the minimum intersubband gap could be traced at the boundary of the Brillouin zone. Differently from these observations, for both the n-n regime ($E > U$) and p-p regime ($E < 0$), the normal order of subbands is well conserved and each subband shows a much stronger dispersion, making the cloning of gapped Dirac points expectable for the periodic modulation. Importantly, without the gate field modulation, the subbands are actually spin independent.

To turn on the spin-dependent subband dispersion, a nonzero Δ_Z should be applied. As shown in Fig. 6(b) for $\Delta_Z = 2\Delta_{SO}$, the nonzero field modulation breaks the spin degeneracy, making the resulting subbands be strongly spin

dependent. Remarkably, for the proper E, e.g., subband near $E/\Delta_{SO} = 7.0$ and 10.5 for the spin-down state (see olive dotted lines) while $E/\Delta_{SO} = 13$ and 18 for the spin-up state (see pink solid lines), only a single subband for a given spin state could be observed. This enables the observation of perfectly spin-polarized transport in the field-tunable BLS system. Moreover, due to the field-enhanced local gap of BLS barriers, the subband dispersion tends to be weakened in the confined regime.

By further increasing Δ_Z to $4\Delta_{SO}$ [see Fig. 6(c)], besides the well-conserved spin-dependent subband structures, another remarkable feature is the emergence of several dispersionless subbands, very much resembling the flat band or atomic-like level. In this case, the dispersionless subbands for E/Δ_{SO} ranging from 14 to 21 can be ascribed to the suppressed interwell coupling since transport through the BLS barrier is evanescent, while those for E/Δ_{SO} ranging from 1 to 4 are mainly induced by the momentum mismatch between the electron-like state in the well and hole-like state in the biased barrier, for which the propagating mode should be expected. These can be also clearly evidenced in Fig. 6(d) for $\Delta_Z = 8\Delta_{SO}$, where evanescent mode-dominant transport in the biased barrier still gives rise to the flat band while that relating to the propagating mode in the biased barrier recovers again its dispersion characteristics. These diverse responses of spin-dependent transport in the biased BLS barrier or superlattice provide flexibly the desirable strategies for BLS-based spinor-electronic applications.

So far with a single-valley approximation, we have demonstrated the field-tunable spin transport in the biased BLS superlattice, but the net signals observed here should cancel each other when both valleys are taken into account. Thus, to rigorously access the spinor-polarized transport in the BLS structures, additional valley or spin-contrasting mechanisms should be included. As far as valley-contrasting mechanisms are concerned, by including the exchange field or circularly polarized light irradiation, it has been theoretically shown for monolayer silicene that the valley-polarized metal phase [35] and even single Dirac cone state [36] are available. Following these demonstrations, the single-valley transport should be also expectable for our BLS system by engineering a fully valley-polarized source via the similar mechanism. Indeed, as recently demonstrated by An et al. [31] for the graphene superlattice, the intervalley scattering induced by the rectangle superlattice barrier results in an unexpected valley-selective Klein tunneling, the valley-contrasting transport, not considered here, and even near-perfected single-valley transport should also be expected for our BLS superlattice by including the intervalley scattering mechanism. As far as the spin-contrasting mechanism is concerned, the incorporation of the ferromagnetic unit, e.g., ferromagnetic BLS induced by the magnetic proximity effect or the use of ferromagnetic electrodes [28,37–39], is a popular method. With a ferromagnetic unit, depending on its magnetization direction, different electrical responses should be recorded for different spin states at a given valley, further providing a direct method to measure the spin-resolved properties when comparing to the valley-dependent optical response [40]. Finally, together with the great achievements for the spin injection and spin-valley locking, our considered structure should also be an efficient

valley modulator once the injection of the spin-polarized beam is achieved.

VI. CONCLUSIONS

We have theoretically investigated electronic transport of massive Dirac fermions in the biased bilayer silicene superlattice in the framework of the four-band effective Hamiltonian. Following the formulated scattering matrix method and single-valley approximation, the field-tunable ballistic transmission probability, conductance, and spin polarization have been systematically studied for the single biased barrier and multiple barriers or the superlattice residing on the bilayer silicene. It is demonstrated that near-perfect polarization and polarization switching could be achieved in the biased bilayer silicene nanostructures via a proper gate field engineering.

Under the one-dimensional periodic field modulation, both the evanescent mode-controlled flat band and propagating mode-controlled flat band are uncovered for the superlattice subbands, and even the perfectly spin-dependent contrast is traced for the spin-dependent subbands of bilayer silicene superlattices. These observations provide the diverse strategies to modulate the spin-valley transport in bilayer silicene for quantum logic applications.

[1] M. M. Waldrop, The chips are down for Moore's law, Nature (London) **530**, 144 (2016).

[2] G. Fiori, F. Bonaccorso, G. Iannaccone, T. Palacios, D. Neumaier, A. Seabaugh, S. K. Baberjee, and L. Colombo, Electronics based on two-dimensional materials, Nat. Nanotechnol. **9**, 768 (2014).

[3] A. K. Geim and K. S. Novoselov, The rise of graphene, Nat. Mater. **6**, 183 (2007).

[4] J. J. Zhao, H. Liu, Z. Yu, R. Quhe, S. Zhou, Y. Wang, C. C. Liu, H. Zhong, and N. Han, Rise of silicene: A competitive 2D material, Prog. Mater. Sci. **83**, 24 (2016).

[5] P. Vogt, P. De Padova, C. Quaresima, J. Aila, E. Frantzeskakis, M. C. Asensio, A. Resta, B. Ealet, and G. Le Lay, Silicene: Compelling Experimental Evidence for Graphenelike Two-Dimensional Silicon, Phys. Rev. Lett. **108**, 155501 (2012).

[6] A. Fleurence, R. Friedlein, T. Ozake, H. Kawai, Y. Wang, and T. Yamada-Takamura, Experimental Evidence for Epitaxial Silicene on Diboride Thin Films, Phys. Rev. Lett. **108**, 245501 (2012).

[7] B. J. Feng, Z. Ding, S. Meng, Y. G. Yao, X. Y. He, P. Cheng, L. Chen, and K. H. Wu, Evidence of silicene in honeycomb structures of silicon on Ag(111), Nano Lett. **12**, 3507 (2012).

[8] L. Meng, Y. Wang, L. Zhang, S. Du, R. Wu, L. Li, Y. Zhang, G. Li, H. Zhou, W. A. Hofer, and H. J. Gao, Buckled silicene formation on Ir(111), Nano Lett. **13**, 685 (2013).

[9] P. De Padova, P. Vogt, A. Resta, J. Avila, I. Razado-Colambo, C. Quaresima, C. Ottaviani, B. Olivieri, T. Bruhn, T. Hirahara, T. Shirai, S. Hasegawa, M. C. Asensio, and G. Le Lay, Evidence of Dirac fermions in multilayer silicene, Appl. Phys. Lett. **102**, 163106 (2013).

[10] E. Noguchi, K. Sugawara, R. Yaokawa, T. Hitosugi, H. Nakano, and T. Takahashi, Direct observation of Dirac cone in multilayer silicene intercalation compound CaSi$_2$, Adv. Mater. **27**, 856 (2015).

[11] P. De Padova, A. Generosi, B. Paci, C. Ottaviani, C. Quaresima, B. Olivieri, E. Salomon, T. Angot, and G. Le Lay, Multilayer silicene: Clear evidence, 2D Mater. **3**, 031011 (2016).

[12] D. Chiappe, E. Scalise, E. Cinquanta, C. Grazianetti, B. van den Broek, M. Fanciulli, M. Houssa, and A. Molle, Two-dimensional Si nanosheets with local hexagonal structure on a MoS$_2$ surface, Adv. Mater. **26**, 2096 (2014).

[13] C. C. Liu, H. Jiang and Y. G. Yao, Low-energy effective Hamiltonian involving spin-orbit coupling in silicene and two-dimensional germanium and tin, Phys. Rev. B **84**, 195430 (2011).

[14] N. D. Drummond, V. Zolyomi, and V. I. Fal'ko, Electrically tunable band gap in silicene, Phys. Rev. B **85**, 075423 (2012).

[15] Z. Y. Ni, Q. H. Liu, K. C. Tang, J. X. Zheng, J. Zhou, R. Qin, Z. X. Gao, D. P. Yu, and J. Lu, Tunable bandgap in silicene and germanene, Nano Lett. **12**, 113 (2012).

[16] C. C. Liu, W. X. Feng, and Y. G. Yao, Quantum Spin Hall Effect in Silicene and Two-Dimensional Germanium, Phys. Rev. Lett. **107**, 076802 (2011).

[17] M. Ezawa, Monolayer topological insulators: Silicene, germanene, and stanene, J. Phys. Soc. Jpn. **84**, 121003 (2015).

[18] M. Ezawa, spin-valley tronics in silicene: Quantum spin Hall–quantum anomalous Hall insulators and single-valley semimetals, Phys. Rev. B **87**, 155415 (2013).

[19] L. Tao, E. Cinquanta, D. Chiappe, C. Grazianetti, M. Fanciulli, M. Dubey, A. Molle, and D. Akinwande, Silicene field-effect transistors operating at room temperature, Nat. Nanotechnol. **10**, 227 (2015).

[20] H. X. Fu, J. Zhang, Z. J. Ding, H. Li, and S. Meng, Stacking-dependent electronic structure of bilayer silicene, Appl. Phys. Lett. **104**, 131904 (2014).

[21] M. Ezawa, Quasi-topological insulator and trigonal warping in gated bilayer silicene, J. Phys. Soc. Jpn. **81**, 104713 (2012).

[22] B. Huang, H. X. Deng, H. Lee, M. Yoon, B. G. Sumpter, F. Liu, S. C. Simth, and S. H. Wei, Exceptional Optoelectronic Properties of Hydrogenated Bilayer Silicene, Phys. Rev. X **4**, 021029 (2014).

[23] F. Liu, C. C. Liu, K. H. Wu, F. Yang, and Y. G. Yao, $d + id'$ Chiral Superconductivity in Bilayer Silicene, Phys. Rev. Lett. **111**, 066804 (2013).

[24] J. J. Liu and W. G. Zhang, Bilayer silicene with an electrically-tunable wide band gap, RSC Adv. **3**, 21943 (2013).

[25] J. G. Rojas-Briseño, M. A. Flores-Carranza, P. Villasana-Mercado, S. Molina-Valdovinos, and I. Rodríguez-Vargas, Tunneling magnetoresistance and spin-valley polarization in magnetic silicene superlattices, Phys. Rev. B **103**, 155431 (2021).

[26] Kh. Shakouri, P. Vasilopoulos, V. Varqiamidis, G.-Q. Hai, and F. M. Peeters, Spin- and valley-dependent commensurability oscillations and electric-field-induced quantum Hall plateaus in periodically modulated silicene, Appl. Phys. Lett. **104**, 213109 (2014).

[27] Q. T. Zhang, K. S. Chan, and J. B. Li, Electrically controllable sudden reversals in spin and valley polarization in silicene, Sci. Rep. **6**, 33701 (2016).

[28] N. Missault, P. Vasilopoulos, F. M. Peeters, B. Van Duppen, Spin- and valley-dependent miniband structure and transport in silicene superlattices, Phys. Rev. B **93**, 125425 (2016).

[29] Z. P. Niu, Y. M. Zhang, and S. H. Dong, Enhanced valley-resolved thermoelectric transport in a magnetic silicene super-lattice, New J. Phys. **17**, 073026 (2015).

[30] B. Van Duppen and F. M. Peeters, Four-band tunneling in bilayer graphene, Phys. Rev. B **87**, 205427 (2013).

[31] X. T. An and W. Yao, Valley-Selective Klein Tunneling through a Superlattice Barrier in Graphene, Phys. Rev. Appl. **14**, 014039 (2020).

[32] H. Q. Xu, Scattering-matrix method for ballistic electron transport: Theory and an application to quantum antidot arrays, Phys. Rev. B **50**, 8469 (1994).

[33] T. Ando, Quantum point contacts in magnetic fields, Phys. Rev. B **44**, 8017 (1991).

[34] Y. Wang, Transfer matrix theory of monolayer graphene/bilayer graphene heterostructure superlattice, J. Appl. Phys. **116**, 164317 (2014).

[35] M. Ezawa, Valley-Polarized Metals and Quantum Anomalous Hall Effect in Silicene, Phys. Rev. Lett. **109**, 055502 (2012).

[36] M. Ezawa, Photoinduced Topological Phase Transition and a Single Dirac-Cone State in Silicene, Phys. Rev. Lett. **110**, 026603 (2013).

[37] Y. Wang, Resonant spin and valley polarization in ferromagnetic silicene quantum well, Appl. Phys. Lett. **104**, 032105 (2014).

[38] D. L. Wang, Z. Y. Huang, Y. Y. Zhang, and G. J. Jin, Spin-valley filter and tunnel magnetoresistance in asymmetrical silicene magnetic tunnel junctions, Phys. Rev. B **93**, 195425 (2016).

[39] X. F. Ouyang, Z. Y. Song, and Y. Z. Zhang, Fully spin-polarized current in gated bilayer silicene, Phys. Rev. B **98**, 075435 (2018).

[40] W. Yao, D. Xiao, and Q. Niu, Valley-dependent optoelectronics from inversion symmetry breaking, Phys. Rev. B **77**, 235406 (2008).